IEEE Access
Multidisciplinary ⋮ Rapid Review ⋮ Open Access Journal

Received 8 March 2023, accepted 25 March 2023, date of publication 31 March 2023, date of current version 19 April 2023.

Digital Object Identifier 10.1109/ACCESS.2023.3263489

RESEARCH ARTICLE

NIRS Data Augmentation Technique to Detect Hemodynamic Peaks During Self-Paced Motor Imagery

ZEPHANIAH PHILLIPS V[1], SEUNG-HO PAIK[1,2], SEUNG-HYUN LEE[3], EUN-JEONG CHOI[4], AND BEOP-MIN KIM[4]

[1]Global Health Technology Research Center, College of Health Science, Korea University, Seoul 02841, Republic of Korea
[2]KLIEN Inc., Seoul Biohub, Seoul 02455, Republic of Korea
[3]Interdisciplinary Program in Precision Public Health, Korea University, Seoul 02841, Republic of Korea
[4]Department of Biomedical Engineering, Korea University, Seoul 02841, Republic of Korea

Corresponding author: Beop-Min Kim (bmk515@korea.ac.kr)

This work was supported in part by the Korea Health Technology Research and Development Project Grant through the Korea Health Industry Development Institute (KHIDI) funded by the Ministry of Health and Welfare, Republic of Korea, under Grant HI14C3477; and in part by the Korea Medical Device Development Fund Grant funded by the Korean Government (Ministry of Science and ICT, Ministry of Trade, Industry, and Energy, Ministry of Health and Welfare, and Ministry of Food and Drug Safety) under Grant KMDF-RS-2022-00140478.

This work involved human subjects or animals in its research. Approval of all ethical and experimental procedures and protocols was granted by the Korea University Institutional Review Board under Approval No. KUIRB-2022-0251-01.

ABSTRACT Optical brain monitoring, such as near-infrared spectroscopy (NIRS), has facilitated numerous brain studies, including those based on machine learning techniques. A large and diverse dataset is necessary for training machine learning algorithms to avoid overfitting a limited amount of data. However, recruiting sufficient subjects is challenging owing to time and budget constraints. Therefore, we propose an NIRS data generation algorithm that scales NIRS signal components, such as hemodynamic response function, physiological systemic noise, and instrumental spike noise, based on the source-detector distance to augment the training data. Experimental self-paced left- and right-hand motor imagery data were augmented with generated NIRS data to train a convolutional neural network and classify the motor imagery data. Augmenting the training dataset with 1000 generated data increased the classification accuracy to 86.3 $\pm$ 4.1%, a 26% increase compared with training on experimental data only. In addition, we applied Guided Gradient-weighted Class Activation Mapping (Grad-CAM) to visualize the class discriminative features of the input data. The peaks of Guided Grad-CAM heatmaps aligned with the oxy-hemoglobin peaks during self-paced motor imagery. We concluded that the increased cerebral oxygenation, especially in the contralateral hemisphere, was the class-discriminative feature for classifying left- and right-hand motor imagery.

INDEX TERMS Cerebral oxygenation, class activation mapping, convolutional neural network, functional near-infrared spectroscopy, machine learning, optical monitoring.

I. INTRODUCTION

Optical brain monitoring with near-infrared spectroscopy (NIRS) can detect increased cerebral oxygenation related to self-paced motor imagery (MI) tasks and accurately classify MI-evoked brain activation [1], [2], [3], [4]. NIRS brain monitoring of MI has led to the development of improved brain–computer interface (BCI) systems for rehabilitation [2], [3], communication and environmental control [2], and real-time neurofeedback [3] to enhance the quality of life for people living with disabilities.

Self-paced MI tasks can be seen as more advantageous than cued MI tasks since the subject can signal the intention of movement at their discretion. However, this freedom

The associate editor coordinating the review of this manuscript and approving it for publication was Md. Kamrul Hasan.

increases the challenges in brain activation analysis. Since the exact occurrence of imagery is unknown, detecting MI and discriminating between types of MI (i.e., left-hand motor imagery (LMI) and right-hand motor imagery (RMI)) is a more complex task. Machine learning algorithms, such as convolutional neural networks (CNNs), offer an automated method to analyze and classify MI tasks by learning class-discriminate features from the dataset [2], [4], [5].

Despite the capabilities of CNNs, gathering sufficient sample data for robust training remains challenging due to the time and budget constraints of recruiting subjects. Insufficient datasets, uneven classes, or biased datasets stemming from a limited number of subjects can lead to overfitting and decrease the accuracy of machine learning algorithms [6].

Data augmentation is one method to increase the number of training data and overcome the issue of limited data sets. Augmentation can be performed via image modifications, such as flipping, translation, scaling, and rotation, to create new data sets [7], [8], [9]. This type of data augmentation can improve classification accuracy [6], [10], but such image manipulations may be irrelevant for channel-encoded two-dimensional input images due to the loss of time-spatial features [11].

To retain the time-spatial features, attention-based layers in the CNN architecture have been shown to preserve physically relevant spatial information and achieve high classification accuracy [12] but do not directly address the biased training that may arise from limited data sets. Alternative augmentation methods have been proposed to increase training data while preserving the time-spatial features. Electroencephalogram (EEG) classification studies of self-paced MI have used frequency shifts, multiplication, and noise additions to increase the number of EEG time-series training data [13]. More comprehensive augmentation techniques include trial averaging, time/frequency recombination, noise addition, cropping, and variational autoencoders [14]. However, these augmentation methods may not apply to very small data sets due to the risk of amplifying biases in the original data set or not correctly representing a wide range of experimental outcomes.

Data generation algorithms offer a more flexible approach for increasing the number of training data by simulating a wide range of experimental scenarios. In the case of NIRS brain monitoring, data generation algorithms are facilitated by accurately modeled functions of NIRS signal components [15], [16]. These studies have proposed techniques for generating realistic NIRS data for discrete near and far source-detector (SD) distances [15], [16]. However, modern high-density NIRS systems often comprise a variety of SD distances that cannot be easily categorized as near or far. Since SD can determine a channel's penetration depth, these channels can significantly vary in their sensitivity to physiological changes in noncerebral and cerebral tissue [17]. Therefore, a NIRS data generation algorithm is required to generate individual NIRS signal components according to the SD distance. General adversarial networks have been implemented to generate semi-synthetic NIRS data for a wide range of channels by utilizing subject resting-state data as a basis for the generated data [8]. However, generating entirely synthetic data may be more advantageous for cases where subject data is difficult to obtain.

In addition to the various augmentation methods, the aforementioned studies did not investigate the effect of data augmentation on the CNN training process or identify the class discriminative features in the data set. Since CNNs can localize important features in their convolutional layers [18], [19], class activation mapping (CAM) has been used to visualize the class discriminative features of the input image. [20] Guided Grad-CAM is a type of CAM that uses the back-propagation of gradient weights to visually explain CNN predictions. This method has been used to identify the class discriminative time periods of MI for EEG. [21]. Applying Guided Grad-CAM on time-series NIRS data could identify time-spatial hemodynamic features that may be valuable for understanding brain function during self-paced MI.

In summary, the significant contributions of this work are as follows:

- We propose an algorithm to generate physiologically realistic NIRS data to generate various data sets for a multi-distance probe covering a wide area.
- The generated NIRS data is proposed as an augmentation technique for LMI/RMI experimental data sets to increase the classification accuracy of testing data.
- Guided Grad-CAM is proposed as a method to identify class discriminative features during CNN training and assess the effect of data augmentation on CNN training. To our knowledge, this work is the first application of the Guided Grad-CAM method to observe the class discriminative features in NIRS signals for brain monitoring.

The rest of the paper is organized as follows: Section II reviews the experimental protocol, NIRS system, CNN architecture, and data generation algorithm. Section III covers the results of this work, including examples of generated data, testing accuracy, and visualization of class discriminative features. Section IV discusses the effects of various CNN training parameters on the results. Section V concludes our work by summarizing the significant findings of this study and future potential studies.

II. MATERIALS AND METHODS

A. EXPERIMENTAL PROTOCOL

The experimental protocol, data generation, and training protocol were carefully designed to evaluate and improve the classification accuracy of self-paced LMI/RMI tasks. In this study, 10 (7 males) right-handed subjects (age 29.4 $\pm$ 2.1 years) performed the self-paced MI experiment. The experiment was performed in accordance with the guidelines and approved research plan of the Korea University Institutional Review Board (approval number: KUIRB-2022-0251-01). Informed consent was received from all subjects. The experiment design is shown in Fig. 1(A).

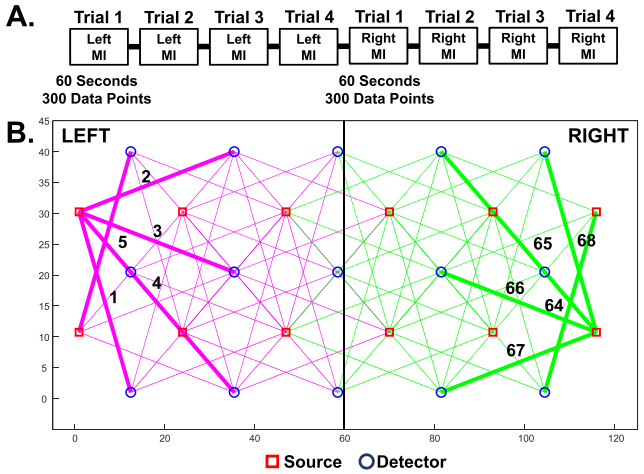

FIGURE 1. (A) Experiment protocol for LMI and RMI. (B) Channel layout for the 68 channels with SD distances of 30, 36, and 45 mm. The channels are numbered according to their spatial location. The first and last five channels are highlighted for reference.

Each trial lasted 60 s (approximately 300 data points), with a 30 s rest before each trial. The subjects were asked to imagine pressing the "F" and "E" keys on a keyboard for LMI and the "J" and "I" keys for RMI on a standard US keyboard layout. Data from 80 MI trials (eight each for 10 subjects) were used as input for the CNN.

Prior to the experiment, a custom-built NIRS probe was attached to the forehead of the subjects and retained throughout the experiment. Previous NIRS studies have monitored functional brain activation in the prefrontal area during MI, making it a more convenient option than monitoring the motor cortex directly [3]. The bottom row of the detectors was aligned to the Fp1-Fpz-Fp2 line (Fig. 1(B)), and the subjects were instructed to avoid large head movements throughout the experiment.

B. NIRS SYSTEM

The NIRS system in this study is the same as that used in previous clinical NIRS studies [22], [23], [24] (Fig. 1(B)). The system includes 12 photodetectors and 15 LED light sources (760 and 850 nm wavelengths) for 108 channels with SD distances of 15, 32, 36, and 45 mm. Appropriate light intensity levels are validated before starting each experiment. A custom-built NIRS data acquisition and processing software was built in MATLAB 2013b (The MathWorks, Inc., Natick, MA, US). After data acquisition, the light intensity changes are converted into optical density changes and hemodynamic changes using the modified Beer–Lambert law. [25].

This study considered only oxy-hemoglobin (HbO) changes as they were more pronounced during MI tasks than other hemodynamic measurements [26]. The HbO data were processed with 0.2 Hz low-pass and wavelet detrending filters to remove high-frequency noise and motion artifacts. [27]. HbO data were realigned to zero by subtracting all points from the first point of the trial and then normalized. To remove global hemodynamic interference, the 15 mm channel was used to regress superficial hemodynamics from the 30-, 36-, and 45-mm channels. [28] In total, 68 channels (SD distances of 30, 36, and 45 mm) were used as inputs for the CNN network.

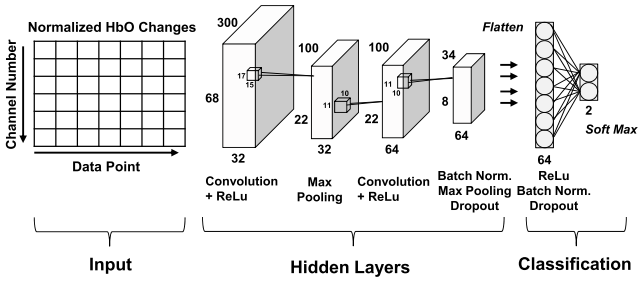

FIGURE 2. Convolution neural network architecture used to classify MI trials. Experimental data augmented with generated NIRS data are used as input.

TABLE 1. CNN architecture.

Operation Layer		Filter Size	Output Image
Input Image		-	68 x 300
Convolution Layer	ReLU	17 x 15	68 x 300 x 32
Pooling Layer	Max Pooling	3 x 3	22 x 100 x 32
Convolution Layer	ReLU	11 x 10	22 x 100 x 64
Batch Normalization	-	3 x 3	22 x 100 x 64
Pooling Layer	Max Pooling	3 x 3	8 x 34 x 64
Dropout	Rate = 0.8	-	8 x 34 x 64
Flatten	-	-	17408
Dense	ReLU	-	64
Batch Normalization	-	-	64
Dropout	Rate = 0.8	-	64
Dense	Softmax	-	2

C. CNN NETWORK

HbO time-series changes from each of the 80 MI trials (40 LMI, 40 RMI) were used as input for the CNN (Fig. 2). The data from each trial are arranged in a two-dimensional image: 68 channels (y-axis) by 300 data points (x-axis). The channels were arranged according to the channel number based on probe position. The first and last five (1–5; 64–68) channels on the left and right positions are shown in Fig. 1 (B).

A description of the CNN architecture is listed in Table 1. The optimizer was Adam (learning rate of 0.0001), the loss function was sparse categorical cross-entropy, and the network was trained with a batch size of 64. The effects of various learning rates, batch sizes, and dropout rates are detailed in *Section* IV *Discussion*.

D. DATA GENERATION ALGORITHM

To augment the training data for the CNN network, we propose a channel-wise NIRS generation algorithm that scales the different NIRS signal components, namely physiological

TABLE 2. Functions to generate components of NIRS signals.

Component	Function	Reference
f_{SYS}	$y_{physiological}(t) = \sum_{t=1}^{4} A_i(t)\sin(2\pi f_i(t)t)$	[15, 16]
f_{HRF}	$h[n] = \alpha(\Gamma[n,\tau_1,t_{01}] - \beta\Gamma[n,\tau_1,t_{01}])$ $\Gamma[n,\tau_x,t_{0x}] = \frac{1}{n!\,\tau_x}\left(\frac{n-t_{0x}}{\tau_x}\right)^b e^{\frac{-(t-t_{0x})}{\tau_x}}$	[15, 16]
f_{SPIKE}	$f(t) = A\exp\left(-\frac{\lvert t-t_0\rvert}{b}\right)$	[29]

TABLE 3. Physiological systemic components frequency range.

Component	Frequency (Hz) Mean ± SD
Cardiac	1.1 ± 0.10
Respiration	0.2 ± 0.03
Mayer	0.07 ± 0.02
Low Frequency	0.01 ± 0.001

systemic noise, instrumental spike noise, and hemodynamic response function (HRF), according to the SD distance.

A near detector can be modeled as scaled physiological systemic noise ($k_1 f_{SYS}$) plus a noise term (ϵ) (Eq (1)). A far detector can be modeled as scaled physiological systemic noise ($k_2 f_{SYS}$) plus a scaled HRF ($k_3 f_{HRF}$) and ϵ term [15] (Eq (2)). However, this model neglects SD distances that cannot be easily categorized as near or far. Therefore, we modified the equations so that each component is a function of the SD distance (d), scaled using an amplitude scaling factor (α_1, α_2, α_3) (Eq (3)).

$$f_{NEAR} = k_1 f_{SYS} + \epsilon \quad (1)$$

$$f_{FAR} = k_2 f_{SYS} + k_3 f_{HRF} + \epsilon \quad (2)$$

$$f_{NIRS}(d) = \alpha_1 f_{SYS} + \alpha_2 f_{HRF} + \alpha_3 f_{SPIKE} + \beta \quad (3)$$

f_{SYS} is the physiological systemic noise due to cardiac, respiration, Mayer wave, and low-frequency oscillations; f_{HRF} is the modeled HRF due to stimulus, and f_{SPIKE} is the instrumental spike noise. β is a Gaussian decay term used to control the HRF width at any given time. The modeling of each component is seen in Table 2.

The exact frequency of f_{SYS} was randomly determined between the range of values used in [15] and summarized in Table 3. The HRF gamma functions were generated using the equation described in [15] such that the HRF shaping variable was set to $[\tau 1, \tau 2] = [0.7, 1.1]$, the scaling variable was set to $[t_{01}, t_{02}] = [5, 0]$, and the undershoot variable was set to $\beta = 0.3$. The amplitude variable of the HRF for the gamma function, α, was randomly set between [1–1.2] for each trial. To generate spike noise, we set the random peak amplitude A between [0.25–1] and the random scale parameter b between [0–0.15].

TABLE 4. Scaling functions for components of generated NIRS signal.

Component	Scaling Function	Input Values
Physiological Systemic Noise (f_{SYS})	$\alpha_1 = A * e^{-\frac{(d-1)}{b_1}}$	$A = 15$ $b_1 = 60$
Hemodynamic Response (f_{HRF})	$\alpha_2 = \frac{1}{1+(e^{\rho*(d-b_2)})}$	$\rho = -0.4$ $b_2 = 15$
Spike Noise (f_{SPIKE})	$\alpha_3 = e^{\frac{d}{b_3}} - 1$	$b_3 = 40$
Gaussian Decay	$\beta = A * e^{-\frac{(d-b_4)^2}{2\sigma^2}}$	$A = 15$ $b_4 = 0$

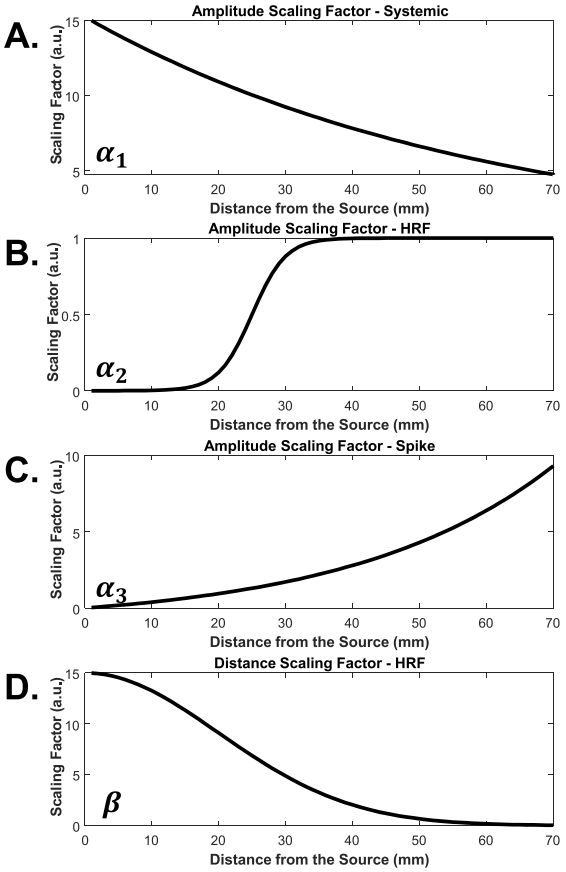

FIGURE 3. Amplitude scaling functions for (A) physiological systemic noise, (B) hemodynamic response function, (C) spike noise, and (D) HRF decay used to generate NIRS data for augmentation. Equations to generate the scaling functions are listed in Table 4.

We modeled each of the amplitude scaling factors (α_1, α_2, α_3, Eq (3)) to adjust the sensitivity for each NIRS signal component according to SD distances (Table 4). The functions comprise seven empirically determined input values that can be adjusted to obtain the desired response.

Scaling was modeled after the Monte Carlo studies of the photon path lengths in the human head [30], [31]. The sensitivity to physiological systemic noise is expected to be highest for shorter SD distances (< 20 mm) and decrease with increasing SD distance (Fig. 3(A)), similar to the previous

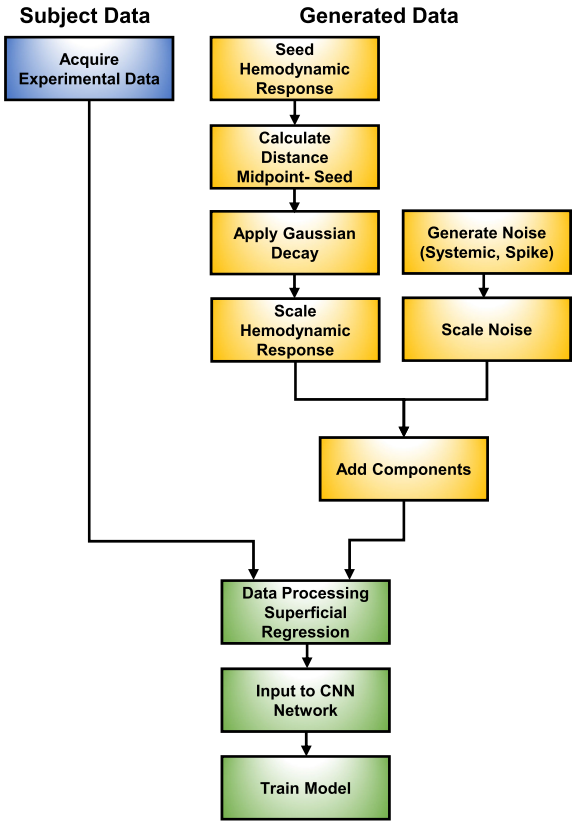

FIGURE 4. Steps to generate NIRS data and data preprocessing for the generated NIRS and experimental data before use in CNN training.

findings on the partial path length of non-brain tissue [30]. Conversely, greater sensitivity to HRF is expected for SD distances greater than 10 mm (Fig. 3(B)), based on the previous findings on the partial path length of brain tissues [30], [31], [32]. As the SD distance increases, an increased spike noise is expected as fewer photons are detected (Fig. 3(C)) [33], [34]. Finally, a gaussian decay term (β in Eq (3)) was applied for the HRF based on the distance between the midpoint of the channel and the center of the HRF seed location (Fig. 3(D)).

The generated NIRS data underwent the same data processing procedure as the experimental data to maintain the same signal conditions between each input data type. This included low-pass filtering, wavelet filtering, near-channel regression, data normalization, and zero realigning at the start of the trial.

An overview of NIRS generation and the data processing workflow is presented in Fig. 4. The first step is to seed the HRF location. Studies have reported that MI brain activation reflects motor execution [35], [36], which is known to have contralateral brain organization [37]. Therefore, the HRF was seeded on the contralateral side of the imagery task. Additionally, the start time and number of HRFs within the trial were randomized for each generated data set. After seeding, the distance from the HRF seed point to the channel midpoint was calculated. The HRF amplitude of each channel was scaled and decayed according to the distance between the midpoint and seed point. Physiological systemic and instrumental spike

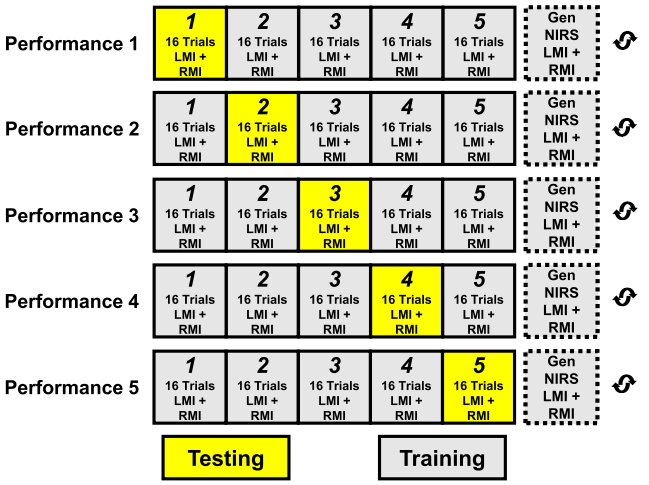

FIGURE 5. Overview of the stratified k-fold training to calculate the network accuracy. The testing and training folds are highlighted in yellow and grey, respectively. The training folds have the generated data shuffled into them. The testing folds determine the accuracy of the CNN network.

noises were generated and scaled before being added to the scaled HRF data. The generated data were then used to augment the experimental data for CNN training.

E. MEASURING ACCURACY AND CLASS ACTIVATION MAPPING

To determine the CNN accuracy, we performed stratified k-fold cross-validation (k = 5) for the training data (Fig. 5). The 80 experimental data points were divided into five folds with an even class distribution. While one fold was used for testing, the others were assigned for training and augmented with an equal distribution of LMI and RMI generated data. The training data were then re-shuffled and trained over 500 epochs. The performance of the 5-fold testing was averaged to determine the overall accuracy. The number of augmented generated data was also increased to observe its effect on classification accuracy. K-fold cross-validation and augmentation with a different amount of generated data was deemed an appropriate way to assess our data augmentation technique's ability to affect classification accuracy.

The Guided Grad-CAM method to visualize class discriminative features was adopted from Keras [38] to construct heatmaps of the input images. Guided Grad-CAM works by back-propagating through the network and observing the gradient flow to reach the target class. [20], [38] The Guided Grad-CAM heatmaps can be used to identify class-discriminative region in the channel-encoded input image which can discern time-spatial hemodynamic features used for classification.

III. RESULTS

The outcomes of this work consist of examples of generated data, testing accuracy according to data augmentation type, and Guided Grad-CAM heatmaps to identify class discriminative features. An example of the generated NIRS data is shown in Fig. 6. The HRF is seeded at the "X" point

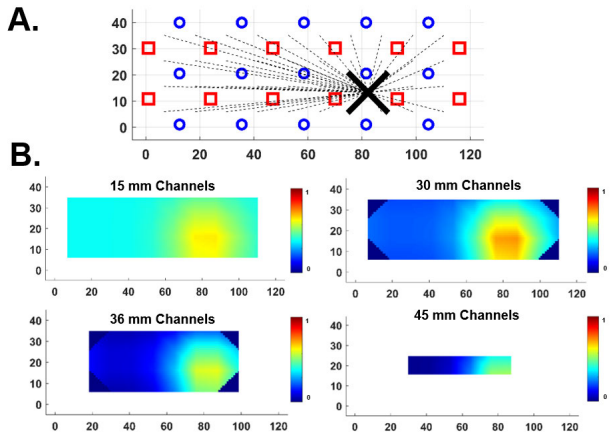

FIGURE 6. Generated NIRS signal based on SD distance. (A) NIRS probe schematic; blue circles and red squares denote the detector and source, respectively. Hemodynamic response originates from the "X" position, and the dashed line represents the distance from the SD midpoint. (B) Topographic HbO reconstruction based on SD distance.

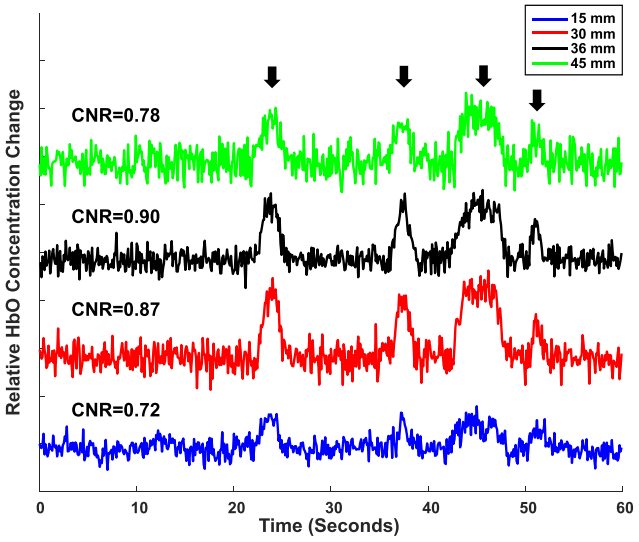

FIGURE 7. Time-series generated NIRS signals based on SD distance. Four hemodynamic response functions are seeded in the generated signals, as denoted by the black arrow.

on the SD layout (Fig. 6(A)). The dotted line signifies the distance between the midpoint and the seed point. Figure 6(B) shows the topographic reconstruction of the HbO changes per SD distance without the regression of the superficial data (15 mm) from the farther channels (30, 36, and 45 mm).

The topographic HbO map for 15 mm shows slight activation due to 15 mm being greater than the recommended distance for observing only systemic components [39]. However, for channels greater than 15 mm, a clear peak of HbO activation at the seed point position is observed, followed by a uniform Gaussian decay away from the seed. In Fig. 6(B), the area of topographic mapping becomes smaller because fewer channels were used to create the map.

The time-series HbO changes of generated data according to SD distance are depicted in Fig. 7, along with the contrast-to-noise ratio (CNR) calculated between the HRF and rest periods [40]. Physiological systemic noise, such as

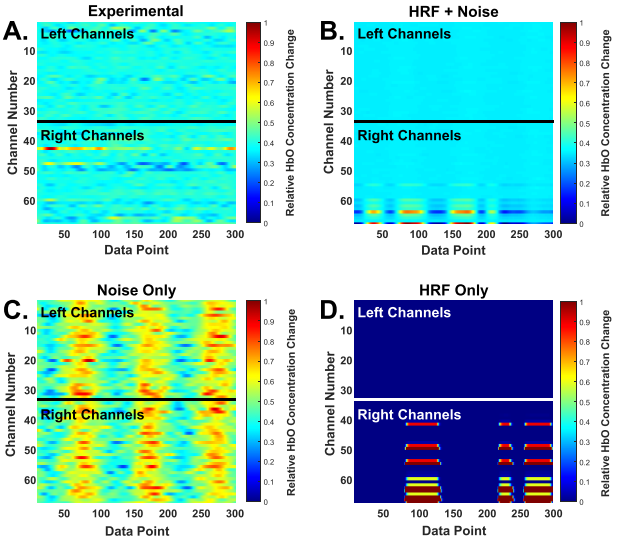

FIGURE 8. Inputs used to train the CNN network. (A) Experimental data of a subject performing left motor imagery. (B) Generated NIRS data of LMI with hemodynamic response and noise (i.e. physiological, spike). (C) Generated NIRS data with physiological and spike noise. (D) Generated NIRS data with only hemodynamic response function.

low frequency oscillations, are most visible at 15 mm. HbO peaks are clearly visible at 30 mm and 36 mm. The peak CNR appearing at SD distances of 30 and 36 mm agrees with the previous findings reporting the highest sensitivity to gray matter changes at a separation of at least 30 mm [30], [31], [32]. At 45 mm, the HbO peaks are less prominent as the spike noise dominates. The agreement of CNR with similar studies at these defined SD distances, along with the visual inspection of the generated data validate that our data generation algorithm can accurately scale components based on SD distances.

To assess the effect of signal components inclusion for the generation algorithm, the training data was augmented with three types of generated data: (1) HRF, physiological systemic noise, instrumental spike noise (HRF + Noise), (2) HRF Only, and (3) physiological, spike noise (Noise Only). The first dataset aims to closely mimic a realistic NIRS signal by including all three major NIRS signal components. The second dataset determines whether the CNN can classify MI with generated data that does not include nonevent-related signals. The third dataset aims to determine the features learned when only nonevent-related noise is present. An individual example of the experimental data, along with the three types of generated data, is shown in Fig. 8.

To validate the generated data's ability to replicate the experimental data, a 5-fold classification was performed on the two data sets with equal distribution of LMI and RMI. The aim is to show that the generated data is indistinguishable from the experimental data. Therefore, the target classification accuracy was set to 50% or a chance level for two classes.

The classification accuracy of the experimental data and HRF Only or Noise Only generated data was 100%. This indicates that CNN could consistently distinguish experimental data from generated data that did not have all three signal

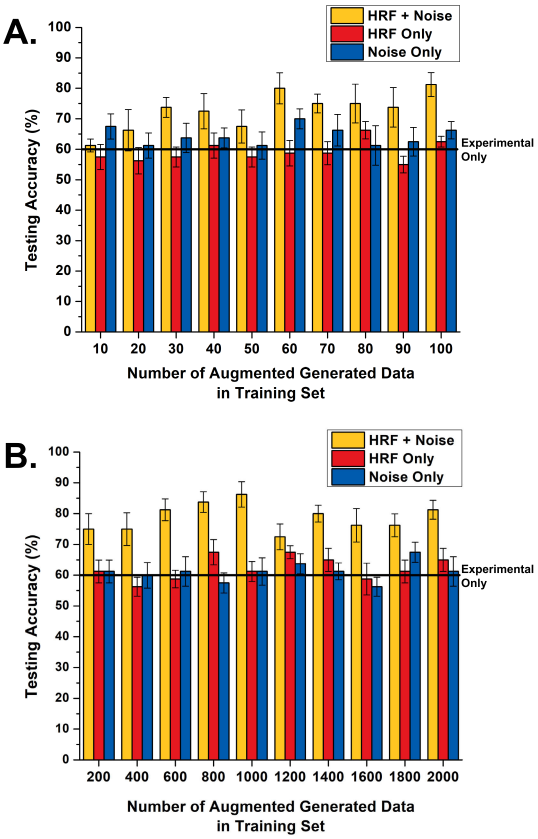

FIGURE 9. Average k-fold accuracy of the testing data according to the number of generated NIRS data augmented to the experimental data in the training set. The number of augmented data between (A) 10–100 and (B) 200–2000. The average testing accuracy using only experimental training data (i.e., with no augmentation) is denoted with a line.

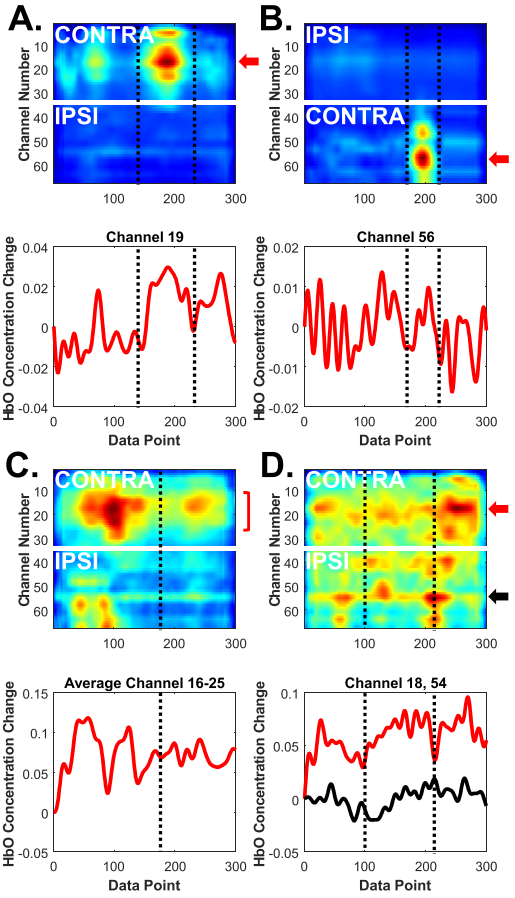

FIGURE 10. Guided Grad-CAM heatmaps (top row) and HbO changes of the activated NIRS channel (bottom row); four individual trials of (A, C, D) right MI and (B) left MI. Channels of interest are denoted by an arrow (top row). The color of the arrow corresponds to the color of the HbO changes (bottom row). (C) HbO changes from channels 16–25 were averaged to correspond to the wide region in the Guided Grad-CAM results.

components. When the generated data was HRF + Noise, the testing accuracy was 87.8%, indicating a small increase in similarity between the experimental and generated data. Future works regarding improving this metric will be discussed in *Section* V *Conclusion*. Although the classification accuracy did not reach the target, the visual confirmation of the generated data (Fig. 7) provides evidence that the data generation algorithm has the intended function.

Next, the effect of data augmentation was observed by performing 5-fold testing for experimental data and experimental data augmented with the three types of generated data. When the CNN was trained with only experimental data, the accuracy was 60 ± 3.79%. This accuracy served as a comparison baseline for assessing the improvement of various augmentation methods. The CNN was trained with augmented data sets, and the testing accuracy was averaged over five folds. The average testing accuracy is shown for the number of augmented data between (*A*) 10 and 100 and (*B*) 200 and 2000.

In case *A* (Fig. 9(A)), a continuous increase in testing accuracy was observed when the training data were augmented with HRF + Noise generated data. The testing accuracy increased to 81.3 ± 3.4% when augmenting the experimental data with 100 generated datasets. The other generated data types (HRF Only and Noise Only) showed no significant difference in accuracy from the baseline.

In case *B,* over a larger number of augmented data (Fig. 9(B)), the testing accuracy peaked at approximately 86.3 ± 4.1% when 1000 HRF + Noise generated data were augmented to the experimental data. Similarly, no increase in testing accuracy was observed when the training data were augmented with the HRF Only or Noise Only generated data. For the number of augmented data greater than 1000, fluctuations in the testing accuracy were observed. This may indicate that a large number of generated data causes the CNN to overfit the generated data.

The peak accuracy of 86.3 ± 4.1% is in line with the previous studies on MI classification using NIRS, which ranged between 77% and 93% [1], [3], [5], [42], [43], [44]. This result demonstrates the capability of our augmentation technique in increasing the testing accuracy of a limited data set to align with similar MI studies. For further experiments, we used the CNN trained with experimental data augmented with 1000 generated data.

The Guided Grad-CAM heatmap analysis can reveal HbO features in the experimental data used to classify LMI and

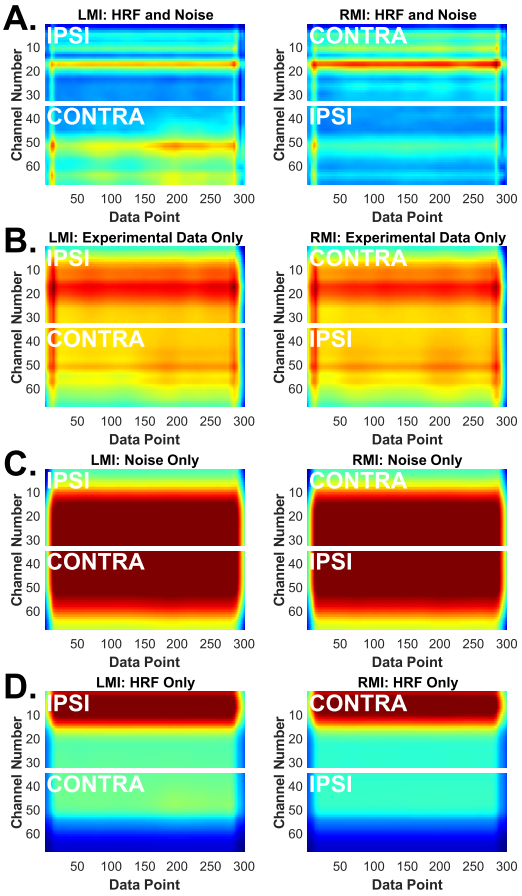

FIGURE 11. Average Guided Grad-CAM heatmaps for the accurately classified trials of left motor imagery (LMI) (left) and right motor imagery (RMI) (right) using a CNN trained with the augmentation of (A) 1000 generated data of HRF and noise (physiological, spike), (B) experimental data only, (C) 1000 generated data of Noise Only, and (D) 1000 generated data of HRF only.

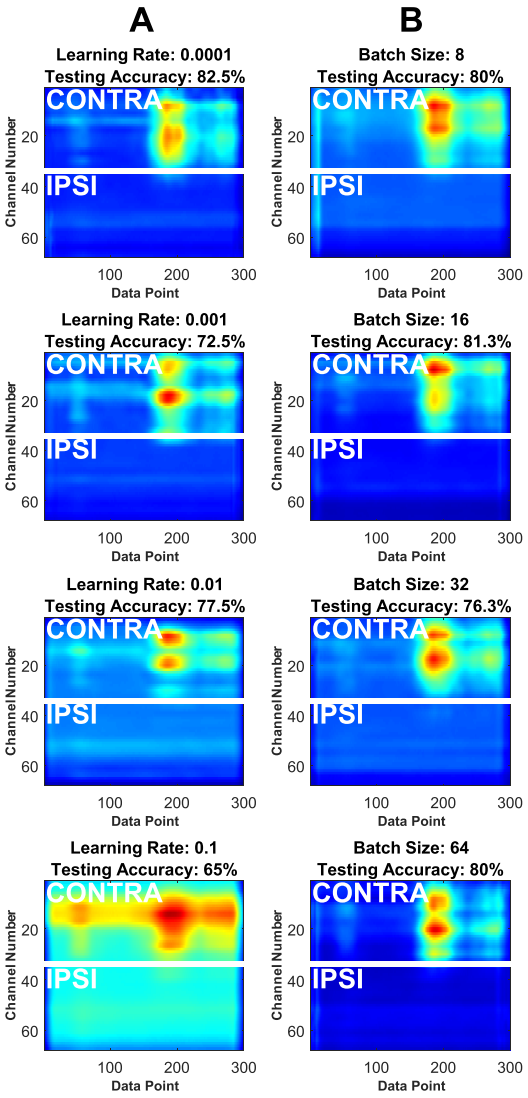

FIGURE 12. Guided Grad-CAM heatmaps and testing accuracy according to (A) learning rate and (B) batch size for one RMI trial. The batch size was fixed to 64 when the learning rate was varied, and the learning rate was fixed to 0.0001 when the batch size was varied.

RMI. Four representative heatmaps from individual subjects are shown in Fig. 10, along with the time series HbO changes from the channel corresponding to the peaks in heatmaps (arrows in Fig. 10). Figs. 10 (A, B) show individual trials of RMI and LMI, respectively, where channel features in the contralateral hemisphere are class-discriminative. The peaks in the heatmap correspond to HbO peaks for this channel which closely resembles our generated HRF (Fig. 7). In Fig. 10(C), the heatmap identifies a large region of time-series data as class-discriminative. Therefore, we averaged the HbO data from the channels in that region (channels 16–25) to show that the peaks in the heatmap correspond to the HbO peaks. Finally, in Fig. 10(D), heatmap peaks are observed in two separate channels (red and black arrows), which also correspond to the HbO peaks in each channel. Figure 10 provides evidence that the CNN network has been trained to detect HbO peaks as a class-discriminative feature for accurate RMI and LMI classification.

We then investigated which cerebral hemisphere showed more class discriminative regions on average for LMI and RMI for all subjects. To do so, we created heatmaps for 80 individual MI trials and then averaged the heat maps for the correctly classified trials (36/40 trials of LMI and 35/40 trials of RMI) (Fig. 11). For LMI and RMI (Fig. 11(A)), the channels on the contralateral hemisphere showed higher average heatmaps results, indicating it contains more class-discriminative regions. These findings are in line with previous motor studies that show the contralateral hemisphere as the discriminative brain region for left and right motor tasks. [36], [43], [44].

For the same trials, we generated heatmaps for a CNN trained with other generated input types (Fig. 11 (B–D)) to validate the ability of our generated data augmentation process to localize class discriminative features. For the three additional input types (Fig. 11 (B–D)), the average heatmaps for LMI and RMI show no distinct patterns of class-discriminative regions. We can conclude that the CNN network trained with other input types cannot converge on

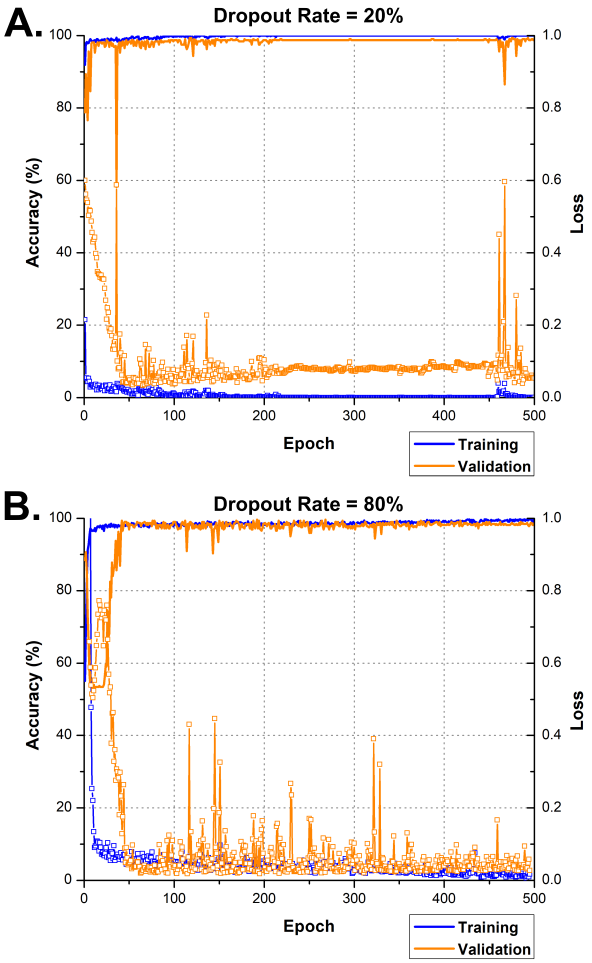

FIGURE 13. Accuracy (left-axis) and loss (right-axis) curves during CNN network training for dropout rates of (A) 20% and (B) 80%. Accuracy (solid line) and loss (square line) are reported for the training (blue) and validation (orange) data sets.

discriminative features in the same manner as HRF + Noise generated data.

IV. DISCUSSION

The training parameters for our CNN were empirically determined; however, for a more comprehensive study, the effect of various CNN training parameters must be discussed. Heatmaps for a single RMI trial according to (A) learning rate and (B) batch size are depicted in Fig. 12. For the highest learning rate of 0.1, the heatmap does not localize a class-discriminative region, and the testing accuracy is the lowest (65%). Conversely, for a lower learning rate of 0.0001, the heatmap localized a class-discriminative region, and the testing accuracy increased to 82.5%. Therefore, the CNN model was trained at a learning rate of 0.0001.

In contrast, various batch sizes show only a small effect on the testing accuracy (Fig. 12(B)), with a maximum accuracy of 81.3% (batch size = 16) and a minimum accuracy of 76.3% (batch size = 32), respectively. However, from our analysis, a larger batch size of 64 resulted in stable heatmaps that were less affected by individual noisy trials. Accordingly, the batch size was set to 64 to train the CNN.

In addition to controlling the learning rate and batch size, the dropout rate for hidden layers can prevent the overfitting of the training data in the CNN network. The prevention of overfitting is critical because it reduces the accuracy of unseen datasets [45]. Fig. 13 shows the accuracy and loss curves of training and validation data during training for dropout rates of 20% (Fig. 13 (A)) and 80% (Fig. 13 (B)). When the dropout rate was set to 80%, some initial instability in the validation classification accuracy was observed, possibly owing to the high dropout rate. However, the accuracy eventually stabilizes to 100%. This early instability is also reflected in the loss curve, with an initial high loss that later converges to a minimum. However, for a 20% dropout rate, the training and validation losses diverge after 100 epochs owing to the increasing validation loss. Divergence is a strong indicator of overfitting toward the training data, resulting in a less accurate classification of the testing data [45]. Hence, we chose a dropout rate of 80% for CNN training.

V. CONCLUSION

The findings of this study contribute toward increasing the classification accuracy of NIRS data for limited sample sizes and identifying class discriminative hemodynamic features for assessing brain function during MI. In this study, the classification accuracy of a limited MI sample was increased from $60 \pm 3.79\%$. to $86.3 \pm 4.1\%$, similar to previous MI studies using NIRS [1, 3, 5, 42–44]. The accuracy was increased by augmenting the training data with generated NIRS data with three major components: HRF, physiological systemic noise, and instrumental spike noise. The classification accuracy only increased when the training data were augmented with generated data that included all three components.

In addition, this study showed the capability of Guided Grad-CAM in visualizing the class discriminative features in NIRS data and observing the effect of data augmentation on CNN training. To our knowledge, this study is the first application of Guided Grad-CAM to detect class discriminative features in time-series NIRS data. The Guided Grad-CAM heatmaps showed that the data augmentation method helped train the CNN to detect the sustained increased cerebral oxygenation in the contralateral hemisphere to classify LMI/RMI. Since increased oxygenation is related to increased brain function, the Guided Grad-CAM method can facilitate the analysis of self-paced tasks to identify spontaneous cerebral activation. The sustained increase of HbO in contralateral channels for LMI and RMI coincides with previous prefrontal brain activation studies during MI tasks [36], [43], [44]. Visual explanations of CNN training for NIRS data can help reduce the black-box nature of machine learning algorithms and identify relevant time-spatial features in the NIRS data for distinguishing MI types.

As discussed in *Section* III *Results*, the scope of our future work would be dedicated to improving the data generation algorithm to better replicate experimental data. Since

classification accuracy only increases when the generated data includes all three major NIRS signal components, we can assume that our augmentation technique works best when the generated data closely resembles the experimental data. However, we observed high classification accuracy between the generated and experimental data, implying that the generated data can be distinguished from experimental data. To improve this metric, further investigations can be done on the benefits of including real subject noise in our generation algorithm to generate semi-synthetic data and closely mimic experimental data. Additionally, rigorous signal decomposition of experimental data can help identify time-frequency distribution and a relevant range of amplitudes for signal components. This can assist in generating realistic frequencies and improving amplitude scaling factors for a more accurate data generation algorithm.

A future study could also assess the effect of additional hemodynamic parameters on CNN training. The coupling of HbO and Hb has been shown to provide more details of neural activity during motor tasks and can bring about new class discriminative features for improved accuracy [46]. Additionally, to further validate the accuracy of our Guided Grad-CAM technique to detect HbO peaks, cross-comparisons can be performed with algorithms capable of automatic peak detection [47].

The ability of the developed data generation algorithm to augment limited data sets and enhance CNN training increases the feasibility of developing highly accurate classifiers based on physiologically relevant features of brain activation. The continual development of NIRS paired with machine learning algorithms can significantly increase the adoption of NIRS monitoring at the clinical level and facilitate the overall interpretation of NIRS signals [48].

REFERENCES

[1] B. Koo, H.-G. Lee, Y. Nam, H. Kang, C. S. Koh, H.-C. Shin, and S. Choi, "A hybrid NIRS-EEG system for self-paced brain computer interface with online motor imagery," *J. Neurosci. Methods*, vol. 244, pp. 26–32, Apr. 2015, doi: 10.1016/j.jneumeth.2014.04.016.

[2] R. Sitaram, H. Zhang, C. Guan, M. Thulasidas, Y. Hoshi, A. Ishikawa, K. Shimizu, and N. Birbaumer, "Temporal classification of multichannel near-infrared spectroscopy signals of motor imagery for developing a brain-computer interface," *NeuroImage*, vol. 34, no. 4, pp. 1416–1427, Feb. 2007, doi: 10.1016/j.neuroimage.2006.11.005.

[3] M. Mihara, N. Hattori, M. Hatakenaka, H. Yagura, T. Kawano, T. Hino, and I. Miyai, "Near-infrared spectroscopy–mediated neurofeedback enhances efficacy of motor imagery–based training in poststroke victims: A pilot study," *Stroke*, vol. 44, no. 4, pp. 1091–1098, Apr. 2013, doi: 10.1161/STROKEAHA.111.674507.

[4] N. Naseer and K.-S. Hong, "Classification of functional near-infrared spectroscopy signals corresponding to the right- and left-wrist motor imagery for development of a brain–computer interface," *Neurosci. Lett.*, vol. 553, pp. 84–89, Oct. 2013, doi: 10.1016/j.neulet.2013.08.021.

[5] T. Trakoolwilaiwan, B. Behboodi, J. Lee, K. Kim, and J.-W. Choi, "Convolutional neural network for high-accuracy functional near-infrared spectroscopy in a brain–computer interface: Three-class classification of rest, right-, and left-hand motor execution," *Neurophotonics*, vol. 5, no. 1, Sep. 2017, Art. no. 011008, doi: 10.1117/1.NPh.5.1.011008.

[6] M. F. Safdar, "A comparative analysis of data augmentation approaches for magnetic resonance imaging (MRI) scan images of Brain tumor," *Acta Inform. Med.*, vol. 28, no. 1, pp. 29–36, 2020, doi: 10.5455/aim.2020.28.29-36.

[7] C. Shorten and T. M. Khoshgoftaar, "A survey on image data augmentation for deep learning," *J. Big Data*, vol. 6, no. 1, pp. 1–48, Dec. 2019, doi: 10.1186/s40537-019-0197-0.

[8] T. Nagasawa, T. Sato, I. Nambu, and Y. Wada, "FNIRS-GANs: Data augmentation using generative adversarial networks for classifying motor tasks from functional near-infrared spectroscopy," *J. Neural Eng.*, vol. 17, no. 1, Feb. 2020, Art. no. 016068, doi: 10.1088/1741-2552/ab6cb9.

[9] J. Nalepa, M. Marcinkiewicz, and M. Kawulok, "Data augmentation for brain-tumor segmentation: A review," *Frontiers Comput. Neurosci.*, vol. 13, p. 83, Dec. 2019, doi: 10.3389/fncom.2019.00083.

[10] P. Chlap, H. Min, N. Vandenberg, J. Dowling, L. Holloway, and A. Haworth, "A review of medical image data augmentation techniques for deep learning applications," *J. Med. Imag. Radiat. Oncol.*, vol. 65, no. 5, pp. 545–563, Aug. 2021, doi: 10.1111/1754-9485.13261.

[11] B. K. Iwana and S. Uchida, "An empirical survey of data augmentation for time series classification with neural networks," *PLoS ONE*, vol. 16, no. 7, Jul. 2021, Art. no. e0254841, doi: 10.1371/journal.pone.0254841.

[12] B. Wang, X. Hu, J. Zhang, C. Xu, and Z. Gao, "Intelligent Internet of Things in mammography screening using multicenter transformation between unified capsules," *IEEE Internet Things J.*, vol. 10, no. 2, pp. 1536–1545, Jan. 2023, doi: 10.1109/JIOT.2022.3209895.

[13] D. Freer and G.-Z. Yang, "Data augmentation for self-paced motor imagery classification with C-LSTM," *J. Neural Eng.*, vol. 17, no. 1, Feb. 2020, Art. no. 016041, doi: 10.1088/1741-2552/ab57c0.

[14] O. George, R. Smith, P. Madiraju, N. Yahyasoltani, and S. I. Ahamed, "Data augmentation strategies for EEG-based motor imagery decoding," *Heliyon*, vol. 8, no. 8, Aug. 2022, Art. no. e10240, doi: 10.1016/j.heliyon.2022.e10240.

[15] R. A. Shirvan, S. K. Setarehdan, and A. M. Nasrabadi, "A new approach to estimating the evoked hemodynamic response applied to dual channel functional near infrared spectroscopy," *Comput. Biol. Med.*, vol. 84, pp. 9–19, May 2017, doi: 10.1016/j.compbiomed.2017.03.010.

[16] N. H. Berivanlou, S. K. Setarehdan, and H. A. Noubari, "Evoked hemodynamic response estimation using ensemble empirical mode decomposition based adaptive algorithm applied to dual channel functional near infrared spectroscopy (fNIRS)," *J. Neurosci. Methods*, vol. 224, pp. 13–25, Mar. 2014, doi: 10.1016/j.jneumeth.2013.12.007.

[17] A. Villringer and B. Chance, "Non-invasive optical spectroscopy and imaging of human brain function," *Trends Neurosci.*, vol. 20, no. 10, pp. 435–442, Oct. 1997, doi: 10.1016/s0166-2236(97)01132-6.

[18] B. Zhou, A. Khosla, A. Lapedriza, A. Oliva, and A. Torralba, "Learning deep features for discriminative localization," in *Proc. IEEE Conf. Comput. Vis. Pattern Recognit. (CVPR)*, Jun. 2016, pp. 2921–2929.

[19] B. Zhou, "Object detectors emerge in deep scene CNNs," in *Proc. ICLR*, 2015, pp. 1–12.

[20] R. R. Selvaraju, M. Cogswell, A. Das, R. Vedantam, D. Parikh, and D. Batra, "Grad-cam: Visual explanations from deep networks via gradient-based localization," *Int. J. Comput. Vis.*, vol. 128, no. 2, pp. 336–359, Oct. 2019, doi: 10.1007/s11263-019-01228-7.

[21] Y. Yan, H. Zhou, L. Huang, X. Cheng, and S. Kuang, "A novel two-stage refine filtering method for EEG-based motor imagery classification," *Frontiers Neurosci.*, vol. 15, Sep. 2021, Art. no. 657540, doi: 10.3389/fnins.2021.657540.

[22] Z. Phillips, J. B. Kim, S.-H. Paik, S.-Y. Kang, N.-J. Jeon, B.-M. Kim, and B.-J. Kim, "Regional analysis of cerebral hemodynamic changes during the head-up tilt test in Parkinson's disease patients with orthostatic intolerance," *Neurophotonics*, vol. 7, no. 4, Oct. 2020, Art. no. 045006, doi: 10.1117/1.NPh.7.4.045006.

[23] J. B. Kim, Z. Phillips, S.-H. Paik, S.-Y. Kang, N.-J. Jeon, B.-J. Kim, and B.-M. Kim, "Cerebral hemodynamic monitoring of Parkinson's disease patients with orthostatic intolerance during head-up tilt test," *Neurophotonics*, vol. 7, no. 2, May 2020, Art. no. 025002, doi: 10.1117/1.NPh.7.2.025002.

[24] Y. H. Kim and Z. Phillips V, "Prefrontal hemodynamic changes measured using near-infrared spectroscopy during the valsalva maneuver in patients with orthostatic intolerance," *Neurophotonics*, vol. 5, no. 1, Jan. 2018, Art. no. 015002, doi: 10.1117/1.NPh.5.1.015002.

[25] D. A. Boas, T. Gaudette, G. Strangman, X. Cheng, J. J. A. Marota, and J. B. Mandeville, "The accuracy of near infrared spectroscopy and imaging during focal changes in cerebral hemodynamics," *Neuroimage*, vol. 13, no. 1, pp. 76–90, Jan. 2001, doi: 10.1006/nimg.2000.0674.

[26] L. Holper, F. Scholkmann, D. E. Shalóm, and M. Wolf, "Extension of mental preparation positively affects motor imagery as compared to motor execution: A functional near-infrared spectroscopy study," *Cortex*, vol. 48, no. 5, pp. 593–603, May 2012, doi: 10.1016/j.cortex.2011.02.001.

[27] B. Molavi and G. A. Dumont, "Wavelet-based motion artifact removal for functional near-infrared spectroscopy," *Physiolog. Meas.*, vol. 33, no. 2, pp. 259–270, Feb. 2012, doi: 10.1088/0967-3334/33/2/259.
[28] R. B. Saager, N. L. Telleri, and A. J. Berger, "Two-detector corrected near infrared spectroscopy (C-NIRS) detects hemodynamic activation responses more robustly than single-detector NIRS," *Neuroimage*, vol. 55, no. 4, pp. 1679–1685, Apr. 2011, doi: 10.1016/j.neuroimage.2011.01.043.
[29] J. W. Barker, A. Aarabi, and T. J. Huppert, "Autoregressive model based algorithm for correcting motion and serially correlated errors in fNIRS," *Biomed. Opt. Exp.*, vol. 4, no. 8, pp. 1366–1379, Aug. 2013, doi: 10.1364/BOE.4.001366.
[30] G. E. Strangman, Z. Li, and Q. Zhang, "Depth sensitivity and source-detector separations for near infrared spectroscopy based on the Colin27 brain template," *PLoS ONE*, vol. 8, no. 8, Aug. 2013, Art. no. e66319, doi: 10.1371/journal.pone.0066319.
[31] G. E. Strangman, Q. Zhang, and Z. Li, "Scalp and skull influence on near infrared photon propagation in the Colin27 brain template," *NeuroImage*, vol. 85, pp. 136–149, Jan. 2014, doi: 10.1016/j.neuroimage.2013.04.090.
[32] G. Taga, F. Homae, and H. Watanabe, "Effects of source-detector distance of near infrared spectroscopy on the measurement of the cortical hemodynamic response in infants," *NeuroImage*, vol. 38, no. 3, pp. 452–460, Nov. 2007, doi: 10.1016/j.neuroimage.2007.07.050.
[33] M. Althobaiti and I. Al-Naib, "Recent developments in instrumentation of functional near-infrared spectroscopy systems," *Appl. Sci.*, vol. 10, no. 18, p. 6522, Sep. 2020.
[34] E. Okada, M. Firbank, M. Schweiger, S. R. Arridge, M. Cope, and D. T. Delpy, "Theoretical and experimental investigation of near-infrared light propagation in a model of the adult head," *Appl. Opt.*, vol. 36, no. 1, pp. 21–31, Jan. 1997, doi: 10.1364/ao.36.000021.
[35] H. H. Ehrsson, S. Geyer, and E. Naito, "Imagery of voluntary movement of fingers, toes, and tongue activates corresponding body-part-specific motor representations," *J. Neurophysiol.*, vol. 90, no. 5, pp. 3304–3316, Nov. 2003, doi: 10.1152/jn.01113.2002.
[36] T. Mulder, "Motor imagery and action observation: Cognitive tools for rehabilitation," *J. Neural Transmiss.*, vol. 114, no. 10, pp. 1265–1278, Oct. 2007, doi: 10.1007/s00702-007-0763-z.
[37] S. H. Johnson, "Cerebral organization of motor imagery: Contralateral control of grip selection in mentally represented prehension," *Psychol. Sci.*, vol. 9, no. 3, pp. 219–222, May 1998, doi: 10.1111/1467-9280.00042.
[38] F. Chollet. (2017). *Grad-CAM Class Activation Visualization*. [Online]. Available: https://keras.io/examples/vision/grad_cam/
[39] S. Brigadoi and R. J. Cooper, "How short is short? Optimum source–detector distance for short-separation channels in functional near-infrared spectroscopy," *Neurophotonics*, vol. 2, no. 2, May 2015, Art. no. 025005, doi: 10.1117/1.NPh.2.2.025005.
[40] X. Cui, S. Bray, and A. L. Reiss, "Functional near infrared spectroscopy (NIRS) signal improvement based on negative correlation between oxygenated and deoxygenated hemoglobin dynamics," *NeuroImage*, vol. 49, no. 4, pp. 3039–3046, Feb. 2010, doi: 10.1016/j.neuroimage.2009.11.050.
[41] X. Yin, "NIRS-based classification of clench force and speed motor imagery with the use of empirical mode decomposition for BCI," *Med. Eng. Phys.*, vol. 37, no. 3, pp. 280–286, Mar. 2015, doi: 10.1016/j.medengphy.2015.01.005.
[42] M. Stangl, G. Bauernfeind, J. Kurzmann, R. Scherer, and C. Neuper, "A haemodynamic brain–computer interface based on real-time classification of near infrared spectroscopy signals during motor imagery and mental arithmetic," *J. Near Infr. Spectrosc.*, vol. 21, no. 3, pp. 157–171, Jun. 2013, doi: 10.1255/jnirs.1048.
[43] K. Kotegawa, A. Yasumura, and W. Teramoto, "Activity in the prefrontal cortex during motor imagery of precision gait: An fNIRS study," *Exp. Brain Res.*, vol. 238, no. 1, pp. 221–228, Jan. 2020, doi: 10.1007/s00221-019-05706-9.
[44] M. Moriya and K. Sakatani, "Effects of motor imagery on cognitive function and prefrontal cortex activity in normal adults evaluated by NIRS," *Adv. Exp. Med. Biol.*, vol. 977, pp. 227–231, Jan. 2017, doi: 10.1007/978-3-319-55231-6_31.
[45] N. Srivastava, G. Hinton, A. Krizhevsky, I. Sutskever, and R. Salakhutdinov, "Dropout: A simple way to prevent neural networks from overfitting," *J. Mach. Learn. Res.*, vol. 15, pp. 1929–1958, Jun. 2014.
[46] P. Lachert, D. Janusek, P. Pulawski, A. Liebert, D. Milej, and K. J. Blinowska, "Coupling of oxy- and deoxyhemoglobin concentrations with EEG rhythms during motor task," *Sci. Rep.*, vol. 7, no. 1, pp. 1–9, Nov. 2017, doi: 10.1038/s41598-017-15770-2.
[47] F. Scholkmann, J. Boss, and M. Wolf, "An efficient algorithm for automatic peak detection in noisy periodic and quasi-periodic signals," *Algorithms*, vol. 5, no. 4, pp. 588–603, 2012, doi: 10.3390/a5040588.
[48] Z. V. Phillips, "Functional near-infrared spectroscopy as a personalized digital healthcare tool for brain monitoring," *J. Clinical Neurol.*, vol. 19, pp. 115–124, Mar. 2023, doi: 10.3988/jcn.2022.0406.

ZEPHANIAH PHILLIPS V received the dual B.S. degree in management information systems from the University of Massachusetts–Boston, Boston, USA, and the Frankfurt University of Applied Sciences, Frankfurt, Germany, in 2012, the M.S. degree in information and communications from the Gwangju Institute of Science and Technology, Gwangju, South Korea, in 2015, and the Ph.D. degree in bio-convergence engineering from Korea University, Seoul, South Korea, in 2022. He is currently a Postdoctoral Researcher with Korea University. His research interests include functional near-infrared spectroscopy, diffuse optical tomography, neuroimaging, machine learning, and artificial intelligence.

SEUNG-HO PAIK received the B.S. degree in mechanical engineering from Ajou University, South Korea, in 2009, and the M.S. and Ph.D. degrees in biomedical engineering from Korea University, in 2015 and 2019, respectively. He joined the Global Health Technology Research Center, in 2019. He is a Research Professor with Korea University. He is also a Chief Executive Officer with KLIEN Inc. His research interests include functional near-infrared spectroscopy, medical devices, brain signal analysis, and machine learning.

SEUNG-HYUN LEE received the B.S. and M.S. degrees in electrical engineering and the Ph.D. degree in biomedical engineering from Kyungpook National University, South Korea, in 2006, 2008, and 2018, respectively. From 2008 to 2018, he had spent a research period with the Daegu Gyeongbuk Institute of Science and Technology (DGIST). He was a Postdoctoral Researcher with the Institute of Biomedical Engineering Research, Kyungpook National University, in 2019. He is currently a Research Professor with Korea University, Seoul, South Korea. His research interests include functional near-infrared spectroscopy, brain signal processing, and machine learning.

EUN-JEONG CHOI received the B.S. degree in mechatronics engineering from Dongseo University, Busan, South Korea, in 2020. She is currently pursuing the integrated master's and Ph.D. degree with the Department of Biomedical Engineering, Korea University, Seoul, South Korea. Her research interests include signal processing for improving fNIRS signals and deep learning.

BEOP-MIN KIM received the B.S. degree in mechanical engineering from Korea University, Seoul, South Korea, in 1989, and the M.S. and Ph.D. degrees in bioengineering from Texas A&M University, College Station, TX, USA, in 1991 and 1996, respectively.

He was recently elected as the CEO of the Korea Medical Device Development Foundation (KMDF), which invests U.S.$ 1 billion in medical device research in South Korea. From 1993 to 1996, he was a Predoctoral Fellow with the M.D. Anderson Cancer Center, University of Texas, Houston, TX, USA, and the University of Texas Medical Branch, Galveston, TX, USA. From 1996 to 2001, he was with the Medical Technology Program, Lawrence Livermore National Laboratory, Livermore, CA, USA, where he was a Staff Scientist. From 2001 to 2009, he was an Assistant or Associate Professor with the Department of Biomedical Engineering, Yonsei University, Seoul. He is currently a Professor with the Department of Biomedical Engineering, Korea University. He is the author or coauthor of more than 90 papers in peer-reviewed journals and has made numerous presentations at main national and international conferences and chaired many conferences on biophotonics. His research interests include optical applications in neuroscience, functional near-infrared spectroscopy, and optical microscopy.